Volume 15
Number 25
7 July 2024
Pages 9379–9860

Chemical Science

rsc.li/chemical-science

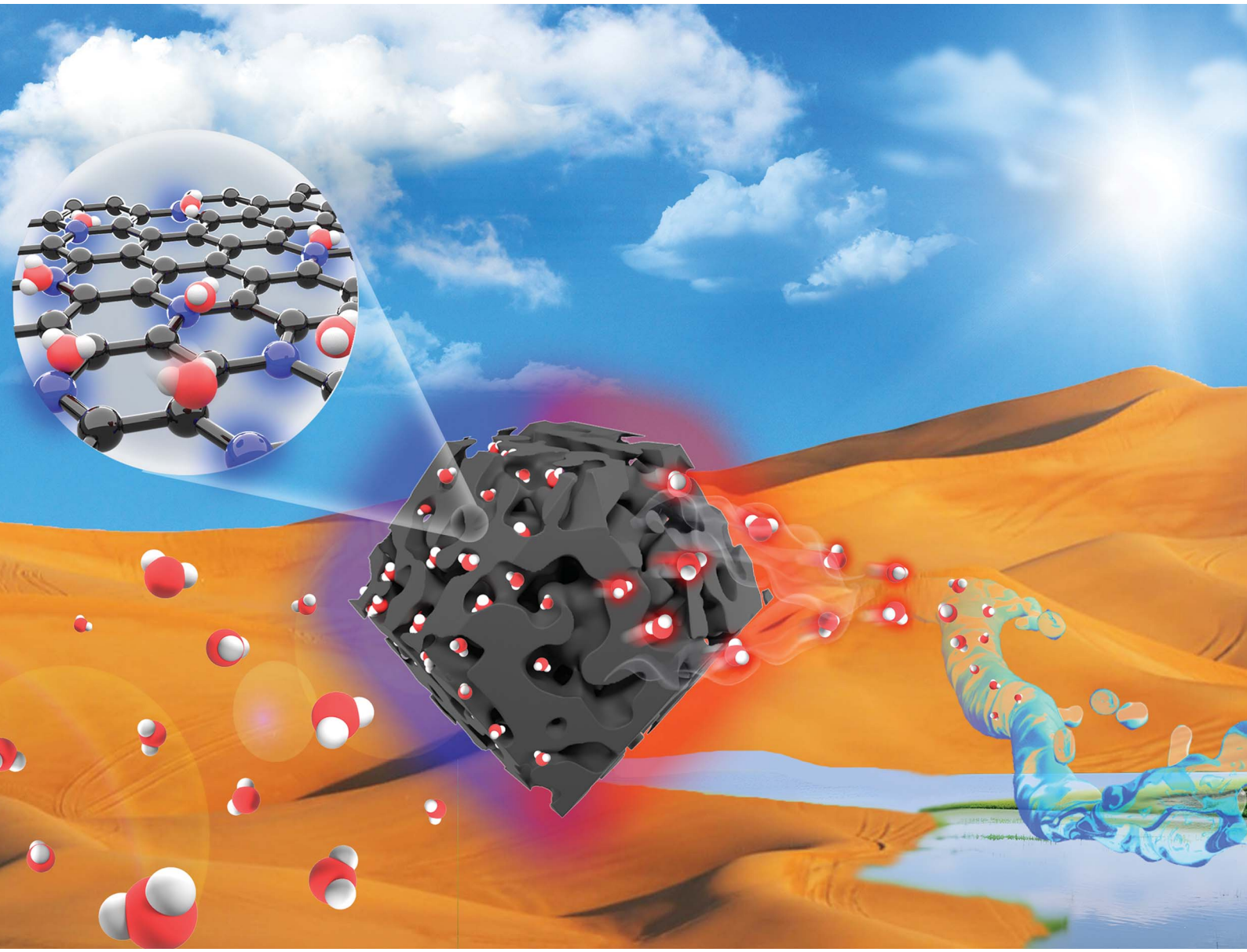

ISSN 2041-6539

ROYAL SOCIETY OF CHEMISTRY

EDGE ARTICLE

Jin-Hua Feng, Feng Lu, Ming Xue, Xiao-Ming Chen *et al.*
Rapid solar-driven atmospheric water-harvesting with MAF-4-derived nitrogen-doped nanoporous carbon

Chemical Science

ROYAL SOCIETY OF CHEMISTRY

EDGE ARTICLE

View Article Online
View Journal | View Issue

Cite this: *Chem. Sci.*, 2024, **15**, 9557

All publication charges for this article have been paid for by the Royal Society of Chemistry

Rapid solar-driven atmospheric water-harvesting with MAF-4-derived nitrogen-doped nanoporous carbon†

Jin-Hua Feng,‡ Feng Lu,‡ Zhen Chen, Miao-Miao Jia, Yi-Le Chen, Wei-Hai Lin, Qing-Yun Wu, Yi Li, Ming Xue * and Xiao-Ming Chen

Sorption-based atmospheric water-harvesting (AWH) could help to solve global freshwater scarcity. The search for adsorbents with high water-uptake capacity at low relative humidity, rapid adsorption–desorption kinetics and high thermal conductivity is a critical challenge in AWH. Herein, we report a MAF-4 (aka ZIF-8)-derived nanoporous carbon (NPC_{MAF-4}-800) with multiple N-doped sites, considerable micropore characteristics and inherent photothermal properties, for efficient water production in a relatively arid climate. NPC_{MAF-4}-800 exhibited optimal water-sorption performance of 306 mg g^{-1} at 40% relative humidity (RH). An excellent sunlight-absorption rate was realized (97%) attributed to its high degree of graphitization. A proof-of-concept device was designed and investigated for the practical harvesting of water from the atmosphere using natural sunlight. NPC_{MAF-4}-800 achieved an unprecedentedly high water production rate of 380 mg g^{-1} h^{-1} at 40% RH, and could produce 1.77 L kg^{-1} freshwater during daylight hours in an outdoor low-humidity climate of ~25 °C and 40% RH. These findings may shed light on the potential of MOF-derived porous carbons in the AWH field, and inspire the future development of solar-driven water-generation systems.

Received 18th March 2024
Accepted 9th May 2024

DOI: 10.1039/d4sc01802h

rsc.li/chemical-science

Introduction

The shortage of fresh potable water is a critical challenge that threatens human health and economic development.[1,2] The atmosphere holds ~13 thousand trillion liters of fresh water in the form of vapor and droplets. Atmospheric water-harvesting (AWH) is an attractive way to capture water vapor from air. Then, the adsorbed water is condensed into liquid water and concentrated in a container.[3,4] Typically, several traditional AWH technologies are utilized for water collection and onsite production. For example, fog collection is achieved by a network of fibers or meshes with macroscopic pores, and water droplets are gathered into a container.[5] Dew condensation can be realized by a refrigerator with the ambient temperature below the dew point, and then the water is condensed from moist air.[6] However, the technologies stated above face major challenges, such as universality under an extremely arid environment.[7,8] In recent years, adsorbent technology based on porous solids, with moisture capture in relatively arid conditions (relative humidity (RH) ≤40%) and exploitation of low-grade energy (*e.g.*, sunlight, waste energy) for desorption, has become an optimal strategy to achieve water-harvesting from the atmosphere on an industrial scale.[9–12] Among them, the adsorption–desorption cycle of AWH systems is dependent upon the water–absorption properties of porous solids at specific humidity. In addition, the rapid adsorption–desorption kinetics of materials have important roles for an increased water yield through more water-harvesting cycles.[13] Recently, one study demonstrated that a tremendous increase in water production could be realized if multiple water-production cycles within 1 day were instigated.[14] Therefore, the development of new porous adsorbents with excellent water uptake and rapid rate of adsorption–desorption could enable the scale-up of AWH systems that work with greater efficiency and productivity.

Several types of porous adsorbents, such as silica gels,[15] zeolites,[16] activated carbon[17] and metal–organic frameworks (MOFs),[18–20] have been investigated for water capture from the atmosphere. Silica gels can achieve high water uptake with large-pore properties. However, due to their hydrophobicity, water uptake is restricted to high RH.[21,22] Zeolites can capture water at relatively low moisture, but the strong interaction between the absorption site and water molecule results in higher energy consumption.[23] Activated carbon can rapidly

School of Chemical Engineering and Technology, School of Chemistry, GBRCE for Functional Molecular Engineering, IGCME, Sun Yat-sen University, Guangzhou, 510275, China. E-mail: xueming5@mail.sysu.edu.cn

† Electronic supplementary information (ESI) available: The SEM image and N_2 adsorption–desorption isotherm, the elemental analysis, the calculation formula of the water adsorption/desorption kinetic; the optical images and operation steps of solar-driven water desorption experiment in the lab environment; the actual operation of indoor AWH device; the demonstration of outdoor atmosphere water harvesting; the water quality analysis by ICP-OES. See DOI: https://doi.org/10.1039/d4sc01802h

‡ These authors contributed equally to this work.

adsorb water molecules onto oxygenated/hydroxylated surface sites, but its saturated water-absorption capacity is relatively low.[24] Among these materials, MOFs have rich porosity, structural diversity, and numerous open sites. Researchers have developed them and their derivatives for AWH.[25–27] Yaghi *et al.* determined the water-filling mechanism of MOF-303 by single-crystal X-ray diffraction (SCXRD). They elucidated that the N heteroatoms of organic linkers have a dominant role as adsorptive sites in a MOF.[28] Yaghi *et al.* developed a multivariate strategy for "tuning" the hydrophilicity, regeneration temperatures and heat of the MOF by introducing active groups.[29] Unfortunately, due to the extremely low photothermal conversion, the MOF usually must be mixed with a solar absorber (*e.g.*, carbon black, CNTs, graphene) to realize passive solar-driven desorption.[30–32] However, the overall energy efficiency is impaired by restrictions elicited by the poor thermal transmission between the water adsorbent and solar absorber.[33] An effective strategy to overcome this shortcoming is the thermal conversion from MOFs to derived nanoporous carbon.[34] Under thermal conversion, the metal species can be easily separated from the backbone, thereby leaving nitrogen heterocyclic rings to blend around metal ions or clusters. Meanwhile, the microporosity of the MOF-derived carbon should be increased further by leaching the metal species with an acid solution. Therefore, MOF-derived carbons obtained through pyrolysis can inherit the intrinsic pore structures of MOF precursors, but also increase the contents of N-doped or O-doped species to improve the affinity of water molecules. More importantly, the additives needed to absorb solar energy in the desorption process can be exempt because of the black colour of derived carbons.

As a typical metal-azolate framework (MAF), zinc(II) 2-methylimidazolate (MAF-4, also known as ZIF-8)[35–37] features a sodalite zeolite-type structure composed of tetrahedral metal ions and imdazolate ligands. MAF-4 has micropores and rich N-containing functional groups.[38,39] Compared with other MOFs, MAF-4 is ideal as a basic precursor for preparing N-doped nanoporous carbon due to its facile and scalable synthesis, as well as the readily available and inexpensive raw material of the 2-methylimidazole ligand. Herein, advanced MAF-4-derived nanoporous carbon ($NPC_{MAF\text{-}4}$-800) with ideal micropore characteristics, rich N-doped species and inherent photothermal properties was obtained for atmospheric water-harvesting (Scheme 1).

Specially, $NPC_{MAF\text{-}4}$-800 displayed a remarkable capacity for water uptake at relatively low humidity, rapid water adsorption/desorption kinetics and excellent photothermal performance. According to the properties stated above, we demonstrated a solar-driven AWH device based on $NPC_{MAF\text{-}4}$-800 realizing the highest water-harvesting rate of 380 mg g^{-1} h^{-1} at 40% RH and achieving 1.77 L kg^{-1} fresh-water production during the daytime outdoors.

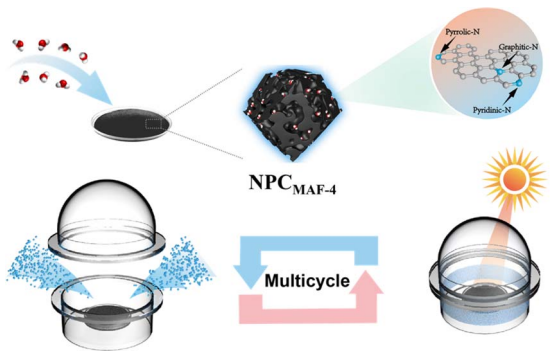

Scheme 1 Water capture with MAF-4-derived N-doped nanoporous carbon ($NPC_{MAF\text{-}4}$) materials and the working principle of a solar-driven atmosphere water-harvesting device (schematic).

Materials and methods

Materials

All chemicals were obtained commercially and used directly without further purification. Zinc nitrate hexahydrate ($Zn(NO_3)_2 \cdot 6H_2O$; purity = 99.0%) was purchased from Xilong Science. 2-Methylimidazole (98.0%) was obtained from Damas-beta. Methanol (AR) was sourced from Macklin. Hydrochloric acid (AR) was purchased from Xilong Science.

Synthesis of MAF-4

$Zn(NO_3)_2 \cdot 6H_2O$ (1.68 g (5.65 mmol)) was added to 80 mL of methanol and stirred for 20 min. In another vial, 3.7 g (45.06 mmol) of 2-methtlimidazole was dissolved in 80 mL of methanol with vigorous stirring. Then, the second solution was added dropwise into the first solution with stirring to form a white suspension. The resulting mixture was stirred at room temperature for 24 h to afford the white crystals of MAF-4. Finally, the crystals were collected by centrifugation and washed thrice with methanol. The resulting MAF-4 was dried at 70 °C before further carbonization.

Synthesis of MAF-4 derived N-doped nanoporous carbon

The carbonization of MAF-4 was realized by direct pyrolysis using a tubular furnace. MAF-4 powders (500 mg) were spread on a quartz vessel, and calcined in a N_2 atmosphere at 700 °C, 800 °C and 900 °C for 2 h in a furnace at a heating rate of 5 °C min^{-1}, respectively. The carbonized products were cooled down to ambient temperature and subsequently pickled in 2 M aqueous HCl solution under stirring for 24 h to remove metal species and residual solvent. After that, the derived carbon was centrifuged and rinsed with deionized water twice. The sample was dried at 70 °C overnight to yield N-doped nanoporous carbons, which were labeled $NPC_{MAF\text{-}4}$-*T*, where *T* represents the carbonization temperature (700, 800 or 900 °C).

Characterization

Powder X-ray diffraction (PXRD) patterns were acquired using a an X-ray diffractometer (Ultima IV; Rigaku) with Cu-Kα (λ = 1.5418 Å) radiation operated at a generator voltage of 40 kV and generator current of 40 mA. Scanning was performed over a range $2\theta = 3–80°$ at $2.0° \cdot min^{-1}$. Scanning electron microscopy (SEM) images were obtained using an Apreo 2S HiVac system (Thermo Fisher Scientific) with an acceleration voltage of 20 kV.

Nitrogen adsorption–desorption isotherms were used to investigate the specific surface area and pore characteristics of samples utilizing a physisorption analyzer (ASAP 2460; Micromeritics) at 77 K. The surface area was calculated using the Brunauer–Emmett–Teller (BET) method at P/P_0 = 0.01–0.3. Pore-size distributions were analyzed by nonlinear density functional theory (NLDFT). Before measurement, the sample was degassed for 24 h at 150 °C under a vacuum. The elemental compositions of samples were determined on an elemental analyzer (EL; Vario). The inherent light absorption of samples was directly characterized by an UV-vis-NIR spectrophotometer (Lambda 950; PerkinElmer). Raman spectroscopy (using 532 nm as the excitation wavelength) on a DXR 2xi System (Thermo Fisher Scientific) was employed to investigate the defect density and molecular configuration of derived carbons. X-ray photoelectron (XPS) studies were conducted on a spectrometer (Nexsa; Thermo Fisher Scientific) with a monochromatic Al-Kα X-ray source, all spectra were calibrated using the C 1s neutral-carbon peak at 284.8 eV. The content of metal ions in water captured by an AWH device was tested through inductively coupled plasma-optical emission spectroscopy (ICP-OES).

Measurement of adsorption of water vapor

Water-sorption experiments were conducted on a gravimetric vapor sorption analyzer (BSD-DVS&VVS; BSD-Sorb) where the humidity was controlled by a mixture of saturated vapor and dry gas in a certain proportion. Initially, ~30 mg of samples were pre-activated at 150 °C for 10 h by *in situ* degassing to ensure complete removal of residual water. Then, they were placed in the crucible of the gravimetric vapor sorption analyzer for adsorption measurement. The weight change after adsorption of water vapor during the measurement was recorded by an electronic balance (accuracy = 0.001 mg) at regular intervals. Each equilibrium value of each corresponding humidity was determined if the weight change was <0.1 mg within 60 min. Dynamic water adsorption–desorption tests were performed on a thermogravimetric module of the BSD-DVS&VVS analyzer. The testing chamber was heated to 150 °C to ensure completely dried NPC_{MAF-4} samples, and then cooled down to 25 °C by an external constant-temperature water-bath under 40% RH for 100 min for water sorption. After sorption, the chamber was heated from 25 °C to 80 °C within 10 min to release water from the samples. The mass changes of samples in the above process were recorded by an internal precision balance in real-time.

Fabrication of a solar-driven AWH device

As shown in Fig. 6b, the atmospheric water-harvester was assembled by an acrylic curved plate, sample vessel and condenser. Among them, the acrylic curved plate was used to condense vapor into liquid water and collect it in the water-collection area by gravity. The glass vessel served to load the adsorbent, and separate the condensate water and samples. The NPC_{MAF-4}-800 sample was weighed and spread out uniformly on the vessel with a sample thickness of ~2 mm. The simulated solar light source utilized a sunlight generator (PLS-SXE300; Perfect Light) with a radiation intensity of 1 kW m^{-2}. The surface temperature of the absorbent was measured by an infrared camera (One Pro; FLIR). The weight change of NPC_{MAF-4}-800 was recorded by an analytical balance at certain time intervals. Environmental conditions were controlled at 25 °C and 40% RH. The collected water capacity was determined by weighing the mass of water preserved in the water-collection area.

Results and discussion

Structure and morphological characterization

Primarily, the purity of the obtained MAF-4 precursor was confirmed by PXRD patterns, SEM and N_2 adsorption test at 77 K (Fig. 1a and S1†).[35] The MAF-4-derived N-doped nanoporous carbons were highly dispersed nanoparticles (size of 100–200 nm) with a polyhedral morphology as revealed by SEM and TEM images (Fig. 2). The prepared NPC_{MAF-4} inherited the original surface structures after carbonization. TEM images of NPC_{MAF-4}-700 and NPC_{MAF-4}-800 revealed amorphous structures with interconnected micropores, but some worm-like mesopores and locally ordered arrangement could be observed in NPC_{MAF-4}-900.[40] Evidently, the interior pore structures of NPC_{MAF-4} derived from MAF-4 could be tuned by regulating the pyrolysis temperature from 700 °C to 900 °C.

As seen in Fig. 1b, the narrow and sharp diffraction peaks of MAF-4 microcrystals changed into broad and low-intensity peaks at ~2θ = 25° and 44° of derived porous carbons. These two peaks were attributed to (002) and (100) crystal planes, suggesting that NPC_{MAF-4} products had typical amorphous structures. With an increase in the thermal treatment temperature, the intensity and degree of these peaks became virtually the same, which confirmed the complete graphitization of NPC_{MAF-4} when the temperature exceeded 700 °C.

The BET surface areas and porosities of MAF-4-derived N-doped nanoporous carbons were characterized by N_2 adsorption–desorption at 77 K. The curves of NPC_{MAF-4}-700 and

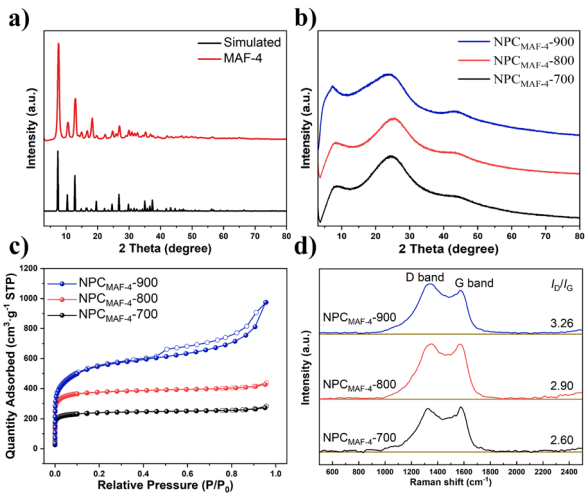

Fig. 1 (a) PXRD patterns of the MAF-4 precursor. Structural characterization of NPC_{MAF-4}. (b) PXRD patterns. (c) N_2 adsorption–desorption isotherms at 77 K. (d) Raman spectra.

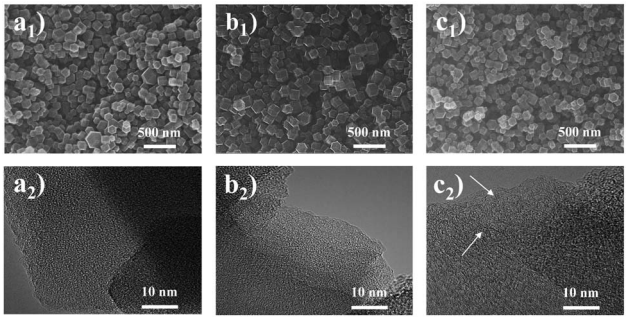

Fig. 2 SEM and TEM images of (a_1, a_2) NPC_{MAF-4}-700, (b_1, b_2) NPC_{MAF-4}-800, and (c_1, c_2) NPC_{MAF-4}-900.

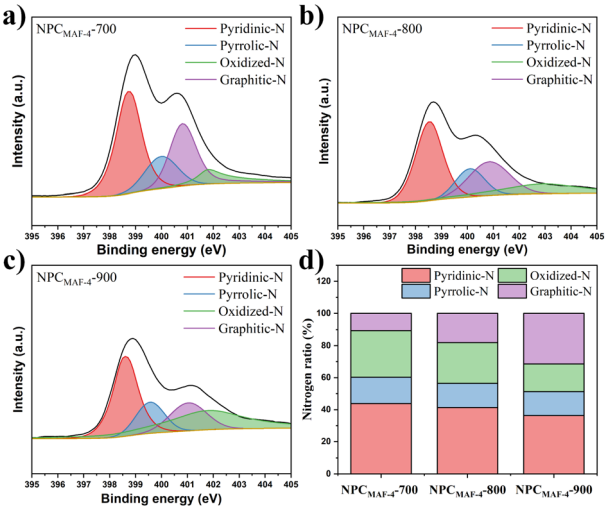

Fig. 3 High-resolution N 1s XPS spectra of (a) NPC_{MAF-4}-700, (b) NPC_{MAF-4}-800, (c) NPC_{MAF-4}-900 and (d) the distribution ratio of N species of NPC_{MAF-4}-*T*.

NPC_{MAF-4}-800 exhibited type-I isotherms with no obvious hysteresis loops (Fig. 1c), which manifested the characteristic of micropores. With an increase in the carbonization temperature from 700 °C to 900 °C, the specific surface area of NPC_{MAF-4} increased gradually from 968 to 2045 $m^2\ g^{-1}$ (Table 1). The micropore ratios of NPC_{MAF-4}-700, -800 and -900 were 44.25%, 72.41% and 26.68%, respectively. The micropore volume accounted for a greater proportion of NPC_{MAF-4}-800 than NPC_{MAF-4}-700 or NPC_{MAF-4}-900. As mentioned above, NPC_{MAF-4}-800 had the highest micropore characteristics and an ideal specific surface area.

To further explore the crystal configurations of MAF-4-derived N-doped nanoporous carbons, Raman spectroscopy was undertaken. As illustrated in Fig. 1d, NPC_{MAF-4} samples were confirmed by spectra showing two bands at 1580 cm^{-1} (G band) and 1360 cm^{-1} (D band), which were attributed to the symmetric bond stretching of a graphitic structure and breathing modes of a disordered structure, respectively.[41,42] The area ratio of the D band to the G band (I_D/I_G) is used to indicate the defect degree of carbon materials. Obviously, the I_D/I_G of NPC_{MAF-4}-700, -800, -900 products were at a high level, suggesting many amorphous defects arising from heteroatomic species after carbonization.[43,44] Furthermore, the values of I_D/I_G increased with an increase in the pyrolysis temperature. This finding indicated that the degree of graphitization of NPC_{MAF-4} was promoted, which could be expected to improve photothermal conversion during solar-driven AWH.

From the perspective of dynamics, the N-doped polar sites from adsorbents may greatly promote low-pressure water absorption, which can induce the formation of water clusters around these sites by hydrogen-bonding interactions.[45] Therefore, the N contents in NPC_{MAF-4} were determined through elemental analysis (Table 1). With an increase in the carbonization temperature, the N content of NPC_{MAF-4} decreased. Specifically, NPC_{MAF-4}-700 and NPC_{MAF-4}-800 exhibited high N contents of 19.58 wt% and 16.62 wt%, respectively, while NPC_{MAF-4}-900 showed the lowest N content of 3.67 wt%. Hence, NPC_{MAF-4}-700 and NPC_{MAF-4}-800 had more abundant N-decorated adsorption sites and increased the affinity of guest molecules. To further clarify the doping types of N element in MAF-4-derived N-doped nanoporous carbons, the XPS spectra of N1s of NPC_{MAF-4}-700, NPC_{MAF-4}-800, NPC_{MAF-4}-900 were investigated in detail (Fig. 3) and the N1s spectra were deconvolved to pyridinic N (398.4 eV), pyrrolic N (399.8 eV), graphitic N (400.9 eV), and oxidized N (402.4 eV). Pyridinic-N and pyrrolic-N species have more affinity with water molecules than other N species.[46,47] Accordingly, XPS showed that the proportion of pyridinic-N and pyrrolic-N species in NPC_{MAF-4} samples were reduced with an increasing pyrolysis temperature. However, the contents of graphitic-N species gradually increased, suggesting that these stable graphitic-N species had been converted from the above two types of nitrogen groups. The contents of pyridinic-N/pyrrolic-N species of NPC_{MAF-4}-700, NPC_{MAF-4}-800, and NPC_{MAF-4}-900 corresponded to 43.86/16.41, 41.34/15.1, and 36.35/14.97 wt%, respectively (Fig. 3d). Given the well-developed micropore structure and strong N-doped adsorbed sites, we considered that NPC_{MAF-4}-800 was a promising N-doped nanoporous carbon for adsorbing water at relatively low humidity.

Table 1 Structural properties of NPC_{MAF-4}-*T*

Samples	S_{BET}[a] $m^2\ g^{-1}$	V_{total}[b] $cm^3\ g^{-1}$	V_{micro}[c] $cm^3\ g^{-1}$	*N* wt%
NPC_{MAF-4}-700	968	0.66	0.29(44.25)	19.58
NPC_{MAF-4}-800	1481	0.66	0.48(72.41)	16.62
NPC_{MAF-4}-900	2045	1.51	0.40(26.68)	3.67

[a] S_{BET} was calculated using a Brunauer–Emmett–Teller (BET) method at $P/P_0 = 0.01$–0.3. [b] V_{total} refers to single-point adsorption of the total pore volume of pores at $P/P_0 = 0.99$. [c] V_{micro} denotes the *t*-Plot micropore volume with a pore size ≤ 2 nm. Values in parentheses represent the proportion of the micropore volume relative to the overall pore volume.

Water–sorption properties

To verify the water-adsorption ability of MAF-4-derived N-doped nanoporous carbon, we evaluated the dynamic vapor sorption (DVS) isotherms of NPC_{MAF-4} samples at 298 K. As shown in Fig. 4a, the water-sorption isotherm of NPC_{MAF-4}-900 showed a type-III curve and a two-step process with the highest

saturated adsorption capacity (746 mg g^{-1} at 95% RH) attributed to its highest specific surface area. However, NPC_{MAF-4}-900 displayed very little water uptake at low RH (below 40% RH). This kind of isotherm was due to a shortage of N-doped sites by the excessive pyrolysis temperature, which resulted in a rather weak interaction between the porous carbon and water molecules. Different from the NPC_{MAF-4}-900 sample, both NPC_{MAF-4}-700 and NPC_{MAF-4}-800 exhibited the type-I isotherm characteristic with no apparent hysteresis. Also, water adsorption increased sharply with increasing pressure until 40% RH due to the strong interaction between water molecules and N-doped polar groups. This finding implied that the abundant micropore structure and more N-doped species were conducive to water absorption at relatively low humidity. Moreover, the subsequent slow adsorption above 40% RH indicated that the micropores and adsorption sites of NPC_{MAF-4}-700 and NPC_{MAF-4}-800 were fully occupied by the adsorbate, along with the weak hydrogen-bonding interactions between the absorbent and water molecules.[48] NPC_{MAF-4}-800 exhibited the highest absorptivity (306 mg g^{-1} at 40% RH), which could be attributed to its superior micropore volume and high N content. Compared with the MAF-4 precursor, NPC_{MAF-4}-800 possessed superior water adsorption (Fig. S2†). To evaluate the recyclability of NPC_{MAF-4}-800, water adsorption/desorption experiments were conducted for seven cycles at 40% RH (Fig. 4b). The water-uptake capacity consistently remained ~306 mg g^{-1}, which aligned with the results for dynamic vapor sorption and illustrated the excellent cyclic stability of NPC_{MAF-4}-800.

The rapid rate of water absorption and desorption at a specific humidity is the key of realizing high-yield water-harvesting. The measurement of water adsorption–desorption dynamics was performed (Fig. 4c). A constant temperature of 25 °C and 40% RH were maintained throughout the sorption process for NPC_{MAF-4}-700 and NPC_{MAF-4}-800. First, the water uptake of NPC_{MAF-4}-700 and NPC_{MAF-4}-800 increased with the adsorption time and reached saturation capacities within 60 min. At 80 °C of the desorption condition (equal to one-solar irradiation), >99% of absorbed water could be released with 30 min for NPC_{MAF-4}-700/800. Notably, the adsorption and desorption kinetics of NPC_{MAF-4}-800 reached 12.50 mg g^{-1} min^{-1} and 10.26 mg g^{-1} min^{-1} within 10 min, respectively, which were 1.53- and 1.44-times faster than those of NPC_{MAF-4}-700 (section S3†). Consequently, the synergistic effect of more accessible porosity and N-doped adsorption sites of NPC_{MAF-4}-800 could explain the outstanding water absorption and release behavior. Prior to the AWH experiment, evaluation of optical absorption by UV-vis-NIR spectra was done (Fig. 4d). NPC_{MAF-4}-800 exhibited a broadband solar adsorption from 300 nm to 2500 nm with an absorptivity of 97%, higher than that of NPC_{MAF-4}-700. These results showed the higher graphitization of NPC_{MAF-4}-800 with more abundant carbon contents, which coincided with the analysis of Raman spectra.

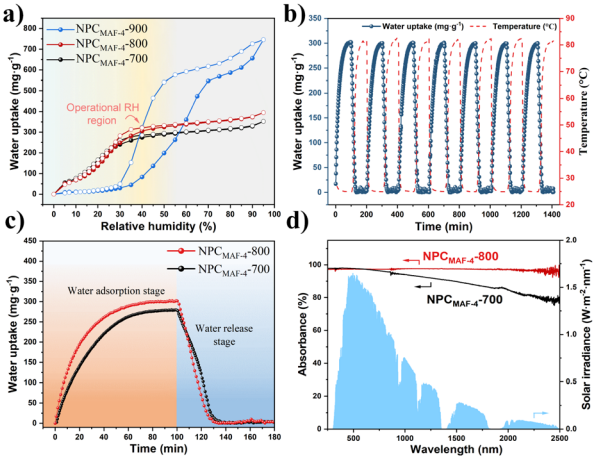

Fig. 4 (a) Water-sorption isotherms at 298 K of NPC_{MAF-4}-*T*. (b) Stability tests of NPC_{MAF-4}-800 over multiple cycles at 40% RH. (c) Dynamic adsorption–desorption performance of NPC_{MAF-4}-700 and NPC_{MAF-4}-800. (d) UV-vis-NIR absorption spectra of NPC_{MAF-4}-700 and NPC_{MAF-4}-800.

Water production of a solar-driven AWH device based on NPC_{MAF-4}-800

First, the light-thermal conversion performance is the most crucial factor for the dehydration rate of samples. Therefore, the desorption capability of NPC_{MAF-4}-800 saturated with water from 40% RH under one-solar irradiation was explored (Fig. S3†). As presented in Fig. 5a and b, the heating temperature rapidly increased and reached 75 °C within 10 min irradiation time under the solar simulator (1 kW m^{-2}), which further verified the result of UV-vis-NIR absorption spectroscopy. In addition, the photothermal properties of NPC_{MAF-4}-800 and MOF-303 mixed with graphene were characterized, and the results showed that the NPC_{MAF-4}-800 exhibited higher surface temperature and heat-transfer efficiency (Fig. S4†). Meanwhile, the adsorption of saturated water in NPC_{MAF-4}-800 could be released by >90% during this period. The rapid desorption of NPC_{MAF-4}-800 is beneficial for inherent photothermal properties, which are superior to conventional solar-driven adsorbents requiring an external light-absorbing medium.[49,50] Building upon the results stated above, the AWH performance of NPC_{MAF-4}-800 based on a proof-of-concept device under indoor conditions powered by one-solar irradiation was tested, and the detailed experimental method is described in the ESI† (Fig. S5 and S6†). To fully realize the maximum daily water productivity of a water-harvester, it is necessary to investigate the optimal operating parameters of the device, such as adsorption time and solar exposure time.[51,52] As shown in Fig. 5c, the results indicated that a time of 10 min adsorption plus 10 min solar irradiation in one cycling test could elicit the highest water production rate of 380 mg g^{-1} h^{-1} at 40% RH with one-solar illumination. This result could be attributed to the high water-uptake capacity at low RH, rapid adsorption–desorption rate and the exceptional photothermal properties of NPC_{MAF-4}-800. These attributes enabled substantial water production throughout entire AWH periods. On the basis of this scheme, the solar-driven AWH application of NPC_{MAF-4}-800 coordinated with a device was tested for 10 cycles to ensure stability during consecutive cycles of water adsorption and desorption. As

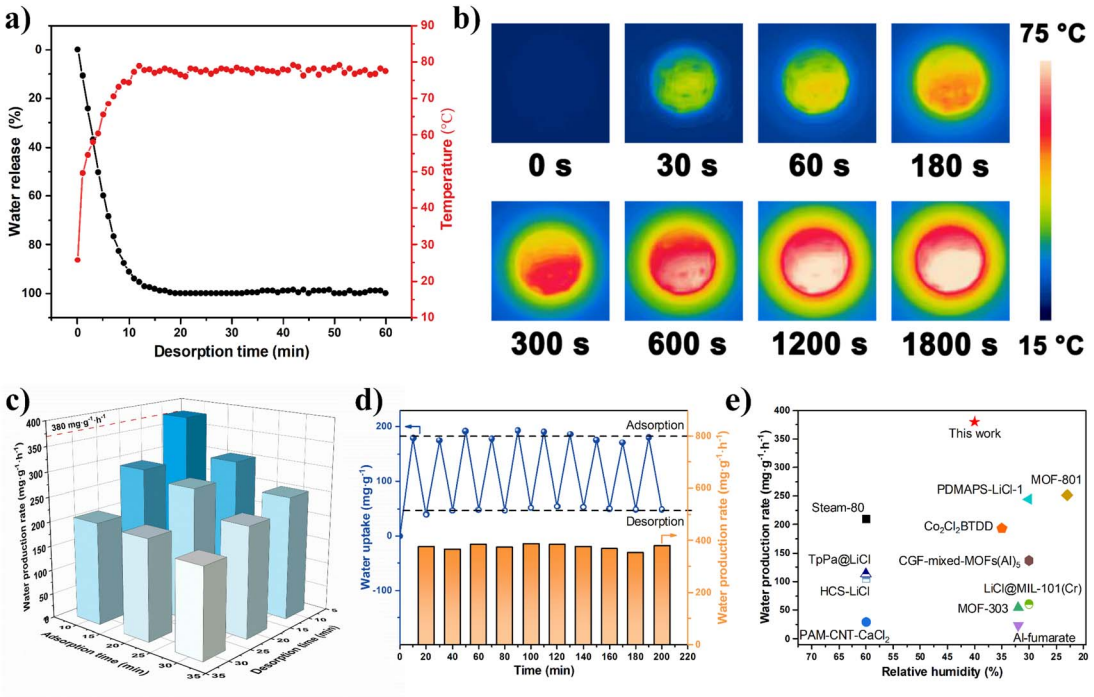

Fig. 5 (a) Time-course of temperature and mass change of saturated adsorbed $NPC_{MAF\text{-}4}$-800 at 40% RH under one-solar irradiation. (b) Time-dependent infrared images of saturated adsorbed $NPC_{MAF\text{-}4}$-800 under one-solar irradiation. (c) Indoor atmosphere water-harvesting of $NPC_{MAF\text{-}4}$-800 at different adsorption and desorption times (adsorption process: 40% RH and 25 °C; desorption process: one-sun illumination). (d) Cycling performance and water-production rate of a solar-driven AWH device based on $NPC_{MAF\text{-}4}$-800. (e) Comparison of the water-production rate and applied humidity with those of representative AWH absorbents.

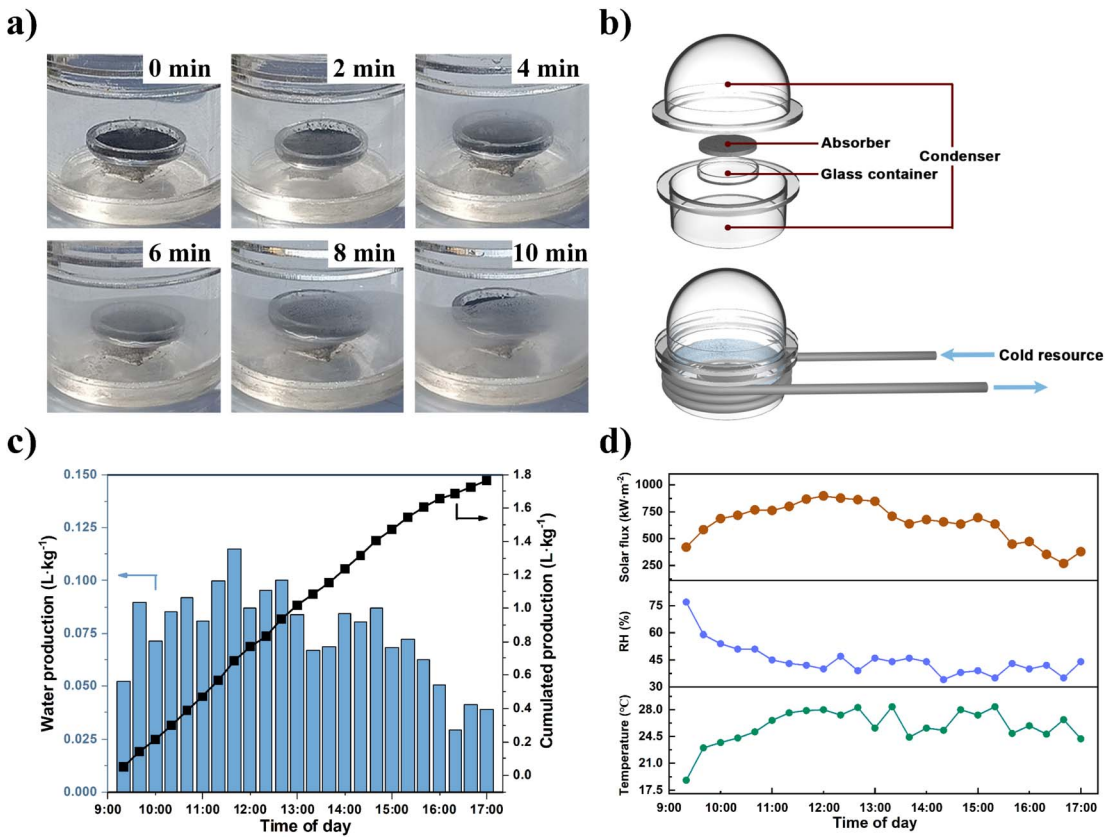

Fig. 6 Performance of outdoor atmosphere water-harvesting and release. (a) Optical image of a device with condensed droplets on inclined walls during water collection. (b) Structure of the AWH device. (c) Freshwater collecting in one daytime *via* 24 sorption–desorption cycles within 8 h. (d) Environment temperature, humidity and solar flux for outdoor water production during daytime.

shown in Fig. 5d, the rate of water production did not show obvious attenuation during 10 cycles, suggesting the outstanding long-term operational stability and adsorption–desorption-reversible properties of $NPC_{MAF\text{-}4}$-800. We compared the water-production rate of $NPC_{MAF\text{-}4}$-800 and other reported state-of-art adsorbents for solar-driven AWH (Fig. 5e and Table S2†). $NPC_{MAF\text{-}4}$-800 achieved the highest water-production rate recorded in a relatively arid condition compared with other solar-driven AWH absorbents reported to date.[30,53–63]

Outdoor AWH demonstration of $NPC_{MAF\text{-}4}$-800

The rapid dynamic AWH performance of $NPC_{MAF\text{-}4}$-800 encouraged us to perform an outdoor field test at the Zhuhai campus of Sun Yat-sen University (SYSU) (22.35° N, 113.59° E) (Section S6†). Specifically, the local ambient air during this period in Zhuhai remained at 30–40% RH and 25 °C. Therefore, a rapid-cycling, solar-driven water-production device was built to validate the practicability of $NPC_{MAF\text{-}4}$-800, which consisted of a vapor condenser, $NPC_{MAF\text{-}4}$-800 absorber in a container, light-transparent cover, supporting plate and water-collecting room (Fig. 6b). To ensure the sorption stage was carried out in the positive direction, we placed the absorber in a dark place for sufficient vapor absorption within 10 min. Then, we moved the AWH device to the outdoor location to perform solar-driven water release and condensation within 10 min to complete one AWH cycle (Fig. S7†). The weather data in the outdoor environment during experimental periods were recorded in real-time (Fig. 6d). The formation, growth and cumulation of droplets on the sidewall within 10 min are shown in Fig. 6a. In the first 2 min, fogging was observed on the window. Subsequently, water vapor accumulated and condensed constantly on the inner walls driven by the temperature difference. After 10 min, many water droplets adhered onto the container wall. Ultimately, the AWH device achieved a cumulative water production of 1.77 L kg^{-1} during daytime (Fig. 6c). To further reduce the energy cost of the device, a second-generation AWH device was powered by solar energy (Fig. S8 and S9†), which also realized satisfactory water production (Fig. S10†). The actual water production of $NPC_{MAF\text{-}4}$-800 was comparable (or even superior) to the values of reported adsorbents under similar climates, such as MOF-303 (0.29 L kg^{-1} day^{-1}),[50] Ni_2Cl_2(BTDD) (0.7 L kg^{-1} day^{-1}),[64] CNF/LiCl aerogel (0.63 L kg^{-1} day^{-1})[65] and Li-SHC (1.09 L kg^{-1} day^{-1}).[66] In addition, the quality of condensate water collected by the outdoor AWH device was checked by ICP-OES by measuring the concentrations of primary metal ion (Fig. S11†). We found that the content of metal ions was below WHO guidelines for drinking-water quality and, thus, suitable for direct potable consumption.[67]

Conclusions

We demonstrated that MAF-4 derived N-doped nanoporous carbons exhibited high water adsorption at low RH, rapid adsorption–desorption kinetics and exceptional photothermal properties for efficient solar-driven AWH. Benefiting from rich N-doped species, ideal micropore characteristics and excellent photothermal properties, $NPC_{MAF\text{-}4}$-800 achieved an outstanding water-uptake capacity of 306 mg g^{-1} at 40% RH and an impressive sunlight absorption rate of 97%. Featuring rapid delivery dynamics and high thermal conductivity, a solar-driven AWH device was created. It realized a superior water-production rate of 380 mg g^{-1} h^{-1} at 40% RH, which is higher than that of previous benchmarks from other solar-driven AWH absorbents reported so far. Moreover, efficient water production of 1.77 L kg^{-1} in the daytime under outdoor conditions was realized. This work reveals the great potential of MOF-derived functional porous carbon materials for freshwater production from the atmosphere by a solar thermal process, which can help solve global water scarcity. Considering this practical solar-driven water enrichment/production, future investigations on the improvement of solar-to-thermal conversion efficiency and sorption dynamics, as well as enhancement of the water production rate of the apparatus, are underway.

Data availability

The data that support the findings of this study are available from the corresponding author upon reasonable request.

Author contributions

Jin-Hua Feng conceptualization: equal; data analysis: equal; investigation: lead; validation: equal; writing (original draft): lead; Feng Lu data analysis: equal; investigation: equal; methodology: lead; writing (original draft): equal; Zhen Chen investigation: supporting; validation: supporting; Miao–Miao Jia data analysis: supporting; investigation: supporting; Yi-Le Chen data curation: supporting; Wei-Hai Lin methodology: supporting; Qing-Yun Wu resources: supporting; Yi Li funding acquisition: supporting; investigation: supporting; Ming Xue funding acquisition: equal; investigation: equal; resources: equal; supervision: lead, writing (review and editing): lead; Xiao-Ming Chen funding acquisition: equal; investigation: equal; resources: equal; writing (review and editing): equal.

Conflicts of interest

The authors declare no conflicts of interest.

Acknowledgements

This work was supported by National Natural Science Foundation of China (22090061, 22071076), Department of Science and Technology of Guangdong Province (2021A1515010204, 2022A1515010021), and Science and technology planning project of Zhuhai (2320004000169).

Notes and references

1 M. M. Mekonnen and A. Y. Hoekstra, *Sci. Adv.*, 2016, **2**, e1500323.
2 J. Eliasson, *Nature*, 2015, **517**, 6.
3 M. Ejeian and R. Z. Wang, *Joule*, 2021, **5**, 1678–1703.

4 A. LaPotin, H. Kim, S. R. Rao and E. N. Wang, *Acc. Chem. Res.*, 2019, **52**, 1588–1597.
5 A. R. Parker and C. R. Lawrence, *Nature*, 2001, **414**, 33–34.
6 M. Muselli, D. Beysens, J. Marcillat, I. Milimouk, T. Nilsson and A. Louche, *Atmos. Res.*, 2002, **64**, 297–312.
7 Y. Zheng, H. Bai, Z. Huang, X. Tian, F.-Q. Nie, Y. Zhao, J. Zhai and L. Jiang, *Nature*, 2010, **463**, 640–643.
8 R. V. Wahlgren, *Water Res.*, 2001, **35**, 1–22.
9 N. Hanikel, M. S. Prévot and O. M. Yaghi, *Nat. Nanotechnol.*, 2020, **15**, 348–355.
10 H. Lu, W. Shi, Y. Guo, W. Guan, C. Lei and G. Yu, *Adv. Mater.*, 2022, **34**, 2110079.
11 Y. Tu, R. Wang, Y. Zhang and J. Wang, *Joule*, 2018, **2**, 1452–1475.
12 T. D. Bennett, F. X. Coudert, S. L. James and A. I. Cooper, *Nat. Mater.*, 2021, **20**, 1179–1187.
13 C. Xiang, F. Deng and R. Wang, *Matter*, 2022, **5**, 2487–2490.
14 F. Fathieh, M. J. Kalmutzki, E. A. Kapustin, P. J. Waller, J. Yang and O. M. Yaghi, *Sci. Adv.*, 2018, **4**, eaat3198.
15 M. R. Manila, S. Mitra and P. Dutta, *Appl. Therm. Eng.*, 2020, **178**, 115552.
16 S. G. Wang, R. Z. Wang and X. R. Li, *Renewable Energy*, 2005, **30**, 1425–1441.
17 Y. Huang, Q. Cheng, Z. Wang, S. Liu, C. Zou, J. Guo and X. Guo, *Chem. Eng. J.*, 2020, **398**, 125557.
18 H. Furukawa, F. Gándara, Y.-B. Zhang, J. Jiang, W. L. Queen, M. R. Hudson and O. M. Yaghi, *J. Am. Chem. Soc.*, 2014, **136**, 4369–4381.
19 T. Yang, L. Ge, T. Ge, G. Zhan and R. Wang, *Adv. Funct. Mater.*, 2021, **32**, 2105267.
20 M. O'Shaughnessy, P. R. Spackman, M. A. Little, L. Catalano, A. James, G. M. Day and A. I. Cooper, *Chem. Commun.*, 2022, **58**, 13254–13257.
21 S. Inagaki, Y. Fukushima, K. Kuroda and K. Kuroda, *J. Colloid Interface Sci.*, 1996, **180**, 623–624.
22 P. L. Llewellyn, F. Schueth, Y. Grillet, F. Rouquerol, J. Rouquerol and K. K. Unger, *Langmuir*, 1995, **11**, 574–577.
23 S. Kayal, S. Baichuan and B. B. Saha, *Int. J. Heat Mass Transfer*, 2016, **92**, 1120–1127.
24 J. Canivet, A. Fateeva, Y. Guo, B. Coasne and D. Farrusseng, *Chem. Soc. Rev.*, 2014, **43**, 5594–5617.
25 S. Bagi, A. M. Wright, J. Oppenheim, M. Dincă and Y. Román-Leshkov, *ACS Sustain. Chem. Eng.*, 2021, **9**, 3996–4003.
26 W. Xu and O. M. Yaghi, *ACS Cent. Sci.*, 2020, **6**, 1348–1354.
27 M. Yuan, M. Gao, Q. Shi and J. Dong, *Chem. Eng. J.*, 2020, **379**, 122412.
28 N. Hanikel, X. Pei, S. Chheda, H. Lyu, W. Jeong, J. Sauer, L. Gagliardi and M. Yaghi Omar, *Science*, 2021, **374**, 454–459.
29 Z. Zheng, N. Hanikel, H. Lyu and O. M. Yaghi, *J. Am. Chem. Soc.*, 2022, **144**, 22669–22675.
30 J. Xu, T. Li, J. Chao, S. Wu, T. Yan, W. Li, B. Cao and R. Wang, *Angew. Chem., Int. Ed.*, 2020, **59**, 5202–5210.
31 B. Wang, X. Zhou, Z. Guo and W. Liu, *Nano Today*, 2021, **40**, 101283.
32 M. Xia, D. Cai, J. Feng, P. Zhao, J. Li, R. Lv, G. Li, L. Yan, W. Huang, Y. Li, Z. Sui, M. Li, H. Wu, Y. Shen, J. Xiao, D. Wang and Q. Chen, *Adv. Funct. Mater.*, 2023, **33**, 2214813.
33 Y. Hu, Z. Fang, X. Ma, X. Wan, S. Wang, S. Fan, Z. Ye and X. Peng, *Appl. Mater. Today*, 2021, **23**, 101076.
34 H.-L. Jiang, B. Liu, Y.-Q. Lan, K. Kuratani, T. Akita, H. Shioyama, F. Zong and Q. Xu, *J. Am. Chem. Soc.*, 2011, **133**, 11854–11857.
35 X.-C. Huang, Y.-Y. Lin, J.-P. Zhang and X.-M. Chen, *Angew. Chem., Int. Ed.*, 2006, **45**, 1557–1559.
36 K. S. Park, Z. Ni, A. P. Côté, J. Y. Choi, R. Huang, F. J. Uribe-Romo, H. K. Chae, M. O'Keeffe and O. M. Yaghi, *Proc. Natl. Acad. Sci. U.S.A.*, 2006, **103**, 10186–10191.
37 J.-P. Zhang, Y.-B. Zhang, J.-B. Lin and X.-M. Chen, *Chem. Rev.*, 2012, **112**, 1001–1033.
38 L. L. Zhuo, P. Chen, K. Zheng, X. W. Zhang, J. X. Wu, D. Y. Lin, S. Y. Liu, Z. S. Wang, J. Y. Liu, D. D. Zhou and J. P. Zhang, *Angew. Chem., Int. Ed.*, 2022, **61**, e202204967.
39 Y. C. Tang, Z. S. Wang, H. Yi, M. Y. Zhou, D. D. Zhou, J. P. Zhang and X. M. Chen, *Angew. Chem., Int. Ed.*, 2023, **62**, e202303374.
40 Z. Y. Sui, Y. N. Meng, P. W. Xiao, Z. Q. Zhao, Z. X. Wei and B. H. Han, *ACS Appl. Mater. Interfaces*, 2015, **7**, 1431–1438.
41 X. Li, C. Hao, B. Tang, Y. Wang, M. Liu, Y. Wang, Y. Zhu, C. Lu and Z. Tang, *Nanoscale*, 2017, **9**, 2178–2187.
42 G.-P. Hao, F. Han, D.-C. Guo, R.-J. Fan, G. Xiong, W.-C. Li and A.-H. Lu, *J. Phys. Chem. C*, 2012, **116**, 10303–10311.
43 A. Li, Y. Tong, H. Song and X. Chen, *J. Phys. Chem. C*, 2018, **122**, 17278–17286.
44 S. Liu, J. Zhou and H. Song, *Small*, 2018, **14**, 1703548.
45 H.-J. Wang, A. Kleinhammes, T. P. McNicholas, J. Liu and Y. Wu, *J. Phys. Chem. C*, 2014, **118**, 8474–8480.
46 T. Matsuoka, H. Hatori, M. Kodama, J. Yamashita and N. Miyajima, *Carbon*, 2004, **42**, 2346–2349.
47 V. A. Cardozo-Mata, J. A. Pescador-Rojas, A. Hernández-Hernández, L. A. Hernández-Hernández, A. Miralrio, F. J. Martínez-Farías, E. Vallejo-Castañeda and E. Rangel, *Appl. Surf. Sci.*, 2020, **502**, 144149.
48 T. Horikawa, N. Sakao, T. Sekida, J. i. Hayashi, D. D. Do and M. Katoh, *Carbon*, 2012, **50**, 1833–1842.
49 G. Yilmaz, F. L. Meng, W. Lu, J. Abed, C. K. N. Peh, M. Gao, E. H. Sargent and G. W. Ho, *Sci. Adv.*, 2020, **6**, eabc8605.
50 W. Song, Z. Zheng, A. H. Alawadhi and O. M. Yaghi, *Nat. Water.*, 2023, **1**, 626–634.
51 X. Wang, X. Li, G. Liu, J. Li, X. Hu, N. Xu, W. Zhao, B. Zhu and J. Zhu, *Angew. Chem., Int. Ed.*, 2019, **58**, 12054–12058.
52 H. Yao, P. Zhang, Y. Huang, H. Cheng, C. Li and L. Qu, *Adv. Mater.*, 2020, **32**, e1905875.
53 Y. Song, N. Xu, G. Liu, H. Qi, W. Zhao, B. Zhu, L. Zhou and J. Zhu, *Nat. Nanotechnol.*, 2022, **17**, 857–863.
54 R. Li, Y. Shi, M. Wu, S. Hong and P. Wang, *Nano Energy*, 2020, **67**, 104255.
55 R. Li, Y. Shi, M. Alsaedi, M. Wu, L. Shi and P. Wang, *Environ. Sci. Technol.*, 2018, **52**, 11367–11377.
56 Y. Wang, W. Chen, J. Fu and Y. Liu, *eScience*, 2023, **3**, 100154.
57 C. Lei, Y. Guo, W. Guan, H. Lu, W. Shi and G. Yu, *Angew. Chem., Int. Ed.*, 2022, **61**, e202200271.

58 H. Kim, S. Yang, S. R. Rao, S. Narayanan, E. A. Kapustin, H. Furukawa, A. S. Umans, O. M. Yaghi and E. N. Wang, *Science*, 2017, **356**, 430–434.
59 H. A. Almassad, R. I. Abaza, L. Siwwan, B. Al-Maythalony and K. E. Cordova, *Nat. Commun.*, 2022, **13**, 4873.
60 H. Kim, S. R. Rao, E. A. Kapustin, L. Zhao, S. Yang, O. M. Yaghi and E. N. Wang, *Nat. Commun.*, 2018, **9**, 1191.
61 A. J. Rieth, S. Yang, E. N. Wang and M. Dinca, *ACS Cent. Sci.*, 2017, **3**, 668–672.
62 F. Luo, T. Liao, X. Liang, W. Chen, S. Wang, X. Gao, Z. Zhang and Y. Fang, *J. Cleaner Prod.*, 2022, **373**, 133838.
63 N. Hanikel, M. S. Prévot, F. Fathieh, E. A. Kapustin, H. Lyu, H. Wang, N. J. Diercks, T. G. Glover and O. M. Yaghi, *ACS Cent. Sci.*, 2019, **5**, 1699–1706.
64 Z. Shao, Z.-S. Wang, H. Lv, Y.-C. Tang, H. Wang, S. Du, R. Sun, X. Feng, P. Poredoš, D.-D. Zhou, J.-P. Zhang and R. Wang, *Appl. Phys. Rev.*, 2023, **10**, 041409.
65 P. Zhu, Z. Yu, H. Sun, D. Zheng, Y. Zheng, Y. Qian, Y. Wei, J. Lee, S. Srebnik, W. Chen, G. Chen and F. Jiang, *Adv. Mater.*, 2023, **36**, e2306653.
66 H. Shan, C. Li, Z. Chen, W. Ying, P. Poredos, Z. Ye, Q. Pan, J. Wang and R. Wang, *Nat. Commun.*, 2022, **13**, 5406.
67 World Health Organization, *Guidelines for Drinking-Water Quality*, 4th edn incorporating the 1st addendum, 2017.